

Entanglement and iSWAP gate between molecular qubits

<https://doi.org/10.1038/s41586-024-08177-3>

Received: 1 July 2024

Accepted: 8 October 2024

Published online: 13 November 2024

 Check for updates

Lewis R. B. Picard^{1,2,3,6}, Annie J. Park^{1,2,3,6}✉, Gabriel E. Patenotte^{1,2,3}, Samuel Gebretsadkan^{1,2,3}, David Wellnitz^{4,5}, Ana Maria Rey^{4,5} & Kang-Kuen Ni^{1,2,3}✉

Quantum computation and simulation rely on long-lived qubits with controllable interactions. Trapped polar molecules have been proposed as a promising quantum computing platform, offering scalability and single-particle addressability while still leveraging inherent complexity and strong couplings of molecules^{1–5}. Recent progress in the single quantum state preparation and coherence of the hyperfine-rotational states of individually trapped molecules allows them to serve as promising qubits^{6–11}, with intermolecular dipolar interactions creating entanglement^{12,13}. However, universal two-qubit gates have not been demonstrated with molecules. Here we harness intrinsic molecular resources to implement a two-qubit iSWAP gate using individually trapped $X^1\Sigma^+$ NaCs molecules. By allowing the molecules to interact for 664 μs at a distance of 1.9 μm , we create a maximally entangled Bell state with a fidelity of 94(3)% in trials in which both molecules are present. Using motion–rotation coupling, we measure residual excitation of the lowest few motional states along the axial trapping direction and find them to be the primary source of decoherence. Finally, we identify two non-interacting hyperfine states within the ground rotational level in which we encode a qubit. The interaction is toggled by transferring between interacting and non-interacting states to realize an iSWAP gate. We verify the gate performance by measuring its logical truth table.

Foundational work three decades ago used molecular systems with nuclear magnetic resonances for proof-of-concept quantum computation^{14,15}, transforming theoretical ideas into early experiments^{16,17}. These platforms used the accessible complexity of molecules, using intrinsic nuclear spins as qubits and natural spin–spin interactions to implement two-qubit gates. However, the platform was difficult to scale and lacked true entanglement¹⁸ because the molecules were dissolved in a solvent at room temperature and subjected to ensemble averaging. Subsequent developments in quantum computing have shifted towards individually controllable systems with simpler structures, such as trapped ions¹⁹, neutral atoms²⁰, and superconducting circuits²¹. Meanwhile, ultracold trapped polar molecules, which have a complex internal structure spanning vibrational, rotational and hyperfine manifolds, were proposed as a new kind of qubit¹. The properties of molecules have been leveraged in recent precision measurements to place improved bounds on the electron electric dipole moment for searches of physics beyond the standard model^{22,23}. These same molecular resources are also expected to prove valuable in quantum science. In particular, the long-range, tunable dipolar interactions between molecules provide a way to perform quantum simulation of exotic quantum phases of matter^{24,25}. For quantum information, the dipolar interaction can be used to implement entangling gates and the rich structure of the molecules enables dense encoding of information, which together may offer a new approach to scalability and fault tolerance^{4,26,27}.

To achieve these goals, ultracold polar molecules have been prepared and isolated in optical traps^{28–30}. In optical tweezer arrays, control and readout of single quantum states of molecules have been achieved^{31–34}, and both hyperfine and rotational coherence have been extended well beyond the dipolar interaction timescale^{6–11}. Most recently, entanglement between two isolated polar molecules has been realized^{12,13}.

In this work, we demonstrate an iSWAP gate, in the class of universal logic gates, to entangle hyperfine states of pairs of individually trapped NaCs molecules. The gate relies on the coherent electric dipole–dipole interaction between rotational states of molecules. We characterize this interaction by creating a two-qubit Bell state within 664 μs with a measured fidelity of 94(3)%, after post-selection to remove trials with empty traps. The fidelity is limited by the motion of molecules along the weakly confined axial dimension of the traps, which we probe using motion–rotation coupling to determine an axial ground state fraction of 34(4)%. We toggle the dipole–dipole interaction on and off by transferring between rotational and nuclear spin degrees of freedom, allowing us to encode qubits in a non-interacting subspace. We measure the truth table of the iSWAP gate, with entanglement inferred from the Bell state fidelity. We identify hyperfine-changing pulses as the dominant source of gate infidelity and offer pathways for near-term improvements. Our results indicate multi-level molecules as viable resources for universal quantum computation and advanced quantum simulations.

¹Department of Chemistry and Chemical Biology, Harvard University, Cambridge, MA, USA. ²Department of Physics, Harvard University, Cambridge, MA, USA. ³Harvard-MIT Center for Ultracold Atoms, Cambridge, MA, USA. ⁴JILA, National Institute of Standards and Technology and Department of Physics, University of Colorado, Boulder, CO, USA. ⁵Center for Theory of Quantum Matter, University of Colorado, Boulder, CO, USA. ⁶These authors contributed equally: Lewis R. B. Picard, Annie J. Park. ✉e-mail: jpark4@fas.harvard.edu; ni@chemistry.harvard.edu

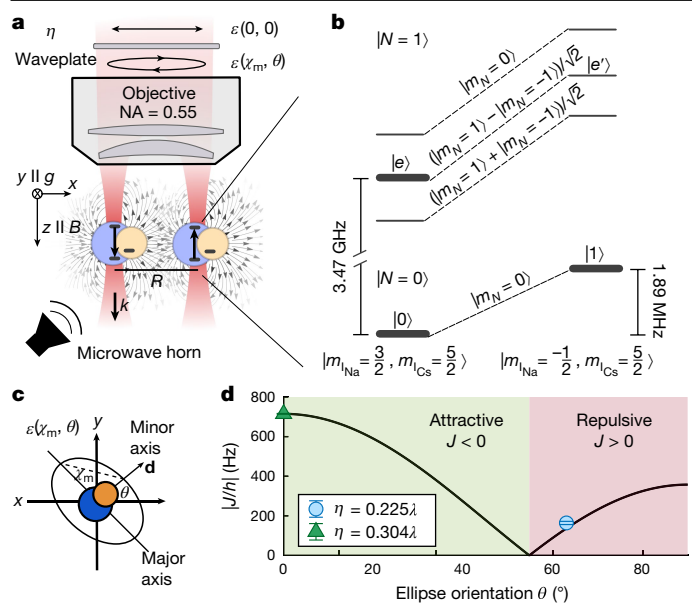


Fig. 1 | NaCs molecules in optical tweezers for dipolar interactions and quantum logic gates. **a**, Schematic of a pair of molecules trapped in neighbouring 1.064 nm optical tweezers. A magnetic field of 863.9 G is applied parallel to the k -vector of the tweezer array, which is along z , and g indicates the direction of gravity. The tweezer polarization $\varepsilon(\chi, \theta)$, defined in the x - y plane by the ellipticity χ and orientation θ , is tuned to a magic ellipticity condition $\varepsilon(\chi_m, \theta)$ using a waveplate with a retardance of η in the path of the initially horizontally polarized light. **b**, Relevant internal states are labelled by their dominant hyperfine states in the rotational ground and first excited manifolds of NaCs. **c**, Illustration of the polarization ellipse in the x - y plane, perpendicular to the k -vector of the tweezer. **d**, Measured interaction strengths J between molecules separated by 1.9 μm at the magic ellipticity condition for two different choices of waveplate retardance η . The black curve shows the expected form of the interaction strength scaled to the maximum value of $|J|/h$ observed at $\eta = 0.304\lambda$. NA, numerical aperture.

Molecular structure

Our experiment starts with a pair of individually trapped NaCs molecules assembled from ground-state-cooled Na and Cs atoms following a procedure detailed previously in ref. 35. These molecules are held in ‘magic’ ellipticity optical tweezers³⁶ in which the polarization ellipticity is chosen to cancel first-order differential light shifts between the $N = 0$ and one sublevel ($|e\rangle$) of the $N = 1$ rotational states, yielding long rotational coherence times³¹. A schematic of the experimental setup is shown in Fig. 1a. Three distinct molecular energy levels, labelled $|0\rangle$, $|1\rangle$ and $|e\rangle$, are important for this work and are shown in Fig. 1b. Molecules are initially assembled in $|0\rangle$ and can be transferred to $|e\rangle$ by resonant microwaves or dipolar exchange. Nuclear spin state $|1\rangle$ in the ground rotational manifold is selected to encode a hyperfine qubit in the molecule, along with the state $|0\rangle$ (see Methods for full state labelling). We sequentially read out $|0\rangle$ and $|e\rangle$ or $|0\rangle$ and $|1\rangle$ in each experimental sequence by converting molecules back to atoms for fluorescence imaging as described in ref. 37. This multi-state readout is essential as it verifies the presence of a molecule in each tweezer independent of its internal state, enabling us to identify cases in which exactly two molecules are detected. The probability of detecting a molecular pair throughout all experimental runs is about 3%, which is primarily limited by the inefficiency of molecule creation³⁷.

A key reason for the choice of NaCs molecules is their large molecule-frame dipole moment of $d = 4.6$ debye (ref. 38). In the absence of an external electric field, the lab-frame permanent dipole moment vanishes. Dipolar interactions then lead to coherent exchange of rotational excitations between pairs of molecules^{10,12,13,39} in the same hyperfine manifold at rate J described by the Hamiltonian^{4,25}

$$\hat{H}_{\text{DD}} = \frac{J}{2} (\hat{s}_1^+ \hat{s}_2^- + \hat{s}_1^- \hat{s}_2^+) = \left(\frac{d}{\sqrt{3}} \right)^2 \frac{1 - 3\cos^2\theta}{4\pi\epsilon_0 R^3} (|0e\rangle\langle e0| + |e0\rangle\langle 0e|), \quad (1)$$

where R is the molecular separation and θ is the angle between the array axis and the transition dipole moment $d/\sqrt{3}$ of the $|0\rangle \leftrightarrow |e\rangle$ transition associated with the raising, $\hat{s}_i^+ = |e\rangle\langle 0|_i$, and lowering, $\hat{s}_i^- = (\hat{s}_i^+)^\dagger$, operators⁴⁰.

The dipolar interaction can be tuned by changing R or θ . Uniquely to our system, the rotational eigenstates of molecules are dominantly quantized by the trapping light rather than static electric or magnetic fields. Therefore, the orientation of the tweezer polarization ellipse (Fig. 1c) determines the angle θ , providing a way to switch between attractive ($J < 0$) and repulsive ($J > 0$) interactions. Experimentally, we realize two different θ s by choosing waveplates with retardances of $\eta = 0.225\lambda$ and 0.304λ while maintaining the magic ellipticity polarization (χ_m) condition (Fig. 1d). For the remainder of this work, we use the latter waveplate to achieve $\theta = 0$, maximizing the magnitude of interaction strength.

Dipole–dipole interaction and entanglement

Coherent dipolar interaction is the essential ingredient required to entangle molecules with high fidelity. We characterize the coherent exchange of rotational excitation between a pair of molecules using a spin-echo Ramsey sequence⁴¹, shown in Fig. 2a (inset). Global microwave pulses are used to address the $|0\rangle \leftrightarrow |e\rangle$ transition. The dipolar exchange interaction results in an output state with amplitudes determined by the interaction time: $|\psi(\tau)\rangle = \frac{1}{2}(1 - e^{-i\frac{J\tau}{\hbar}})|00\rangle + \frac{1}{2}(1 + e^{-i\frac{J\tau}{\hbar}})|ee\rangle$.

Figure 2a shows the evolution of the populations in each of the possible states, $|00\rangle$, $|0e\rangle$, $|e0\rangle$ and $|ee\rangle$, of a pair of molecules separated by 1.9 μm as a function of the total interaction time τ . The data are obtained by post-selection to include only cases in which molecules were detected in both tweezers. We analyse the data with the aid of a master equation simulation of the interaction with decoherence from which we extract an interaction rate of $|J|/h = 715(2)$ Hz (Methods). We observe that the decoherence is dominated by noise on the interaction strength, which can be seen in Fig. 2a by comparing the symmetric decay of the oscillations between $|00\rangle$ and $|ee\rangle$ with the slower rise of the $|0e\rangle$ and $|e0\rangle$ populations. We model this decoherence using a full quantum mechanical simulation of the motion of the molecules. The solid lines represent the decaying oscillations predicted by this model, with parameters extracted from independent single-molecule measurements shown in Fig. 3.

We performed the same experiment at separations of 2.2 μm and 2.5 μm and extracted J for each distance from the master equation simulation (Extended Data Fig. 1 and Extended Data Table 1). Figure 2b shows the interaction rate against the separation and performs a single-parameter fit to the function a/R^3 . We observe good agreement with the expected $1/R^3$ scaling of the dipole–dipole interaction and extract a distance-independent interaction rate of $\frac{|J|}{hR^3} = 5.14(4)$ kHz μm^{-3} . The measured dipolar strength J is the fastest observed in work on ultracold molecules and magnetic atoms, even considering the closer spacings in optical lattice systems^{10,39,42}.

The dipole–dipole interaction natively generates entanglement between the rotational states of the molecules⁴. Applying the spin-echo pulse sequence with an interaction time $|h/2J|$ maps the input $|00\rangle$ product state to the maximally entangled state $\frac{1}{\sqrt{2}}(|00\rangle - |ee\rangle)$, which is equivalent up to a global rotation to the $|\Phi^+\rangle$ Bell states. This was demonstrated experimentally with CaF molecules recently with a fidelity of up to 0.89 (refs. 12,13). We expect our molecules with a large motional ground state fraction to do better. We prepare this maximally entangled state at a molecule separation of 1.9 μm , using an interaction time of 664 μs . To verify the entanglement of the generated state, we measure the off-diagonal coherences of the density matrix by applying

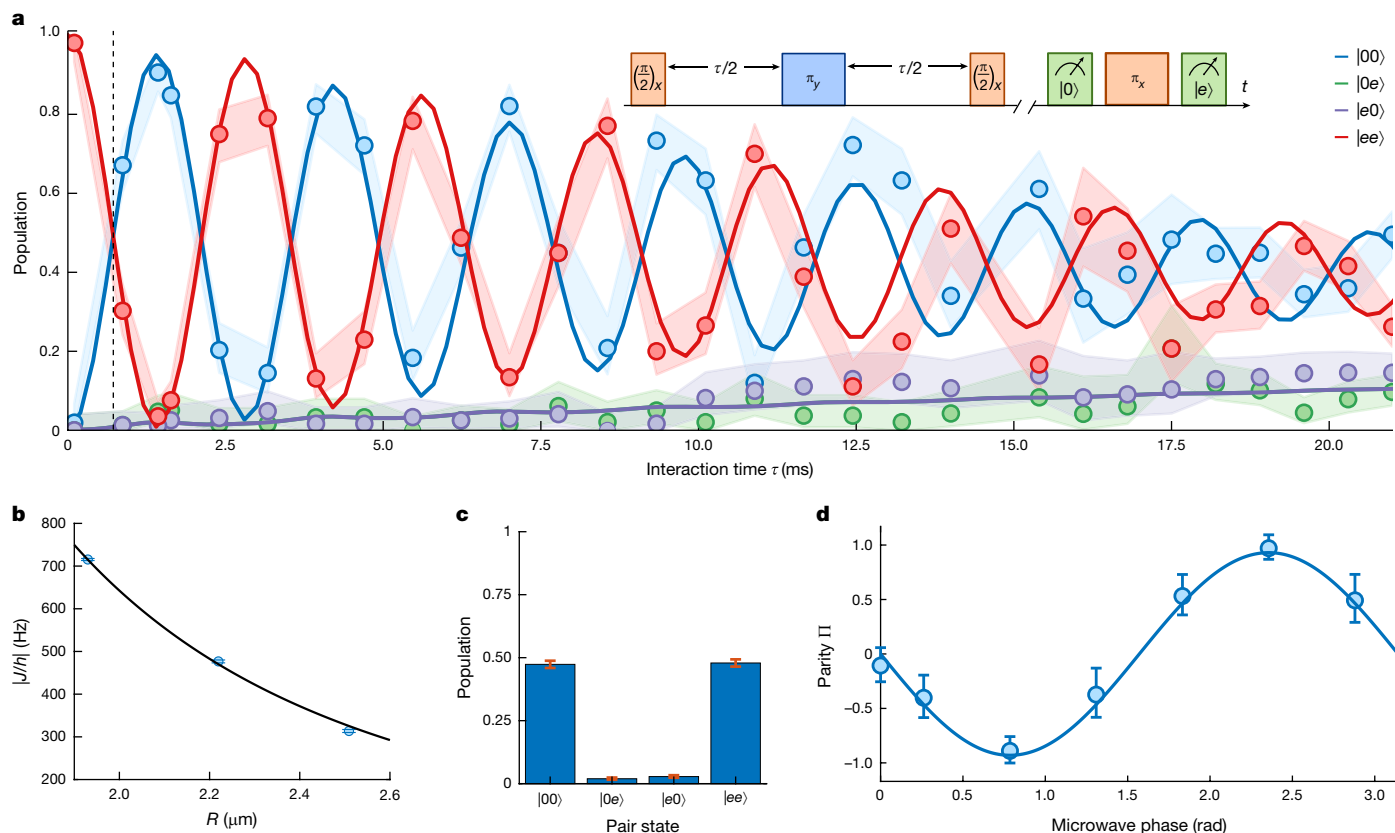


Fig. 2 | Characterization of dipole–dipole-mediated rotational exchange interaction and entanglement, using data obtained by post-selection to include only cases in which both molecules are detected. **a**, Populations of four possible two-molecule states of a pair of molecules undergoing dipolar interaction at a separation of $R = 1.9 \mu\text{m}$. We postselect an average of 61 trials per point in which both molecules are present at the end of the sequence. Each point represents a maximum likelihood estimate of the population of each state and the shaded regions are 1σ confidence intervals. The inset shows the spin-echo microwave pulse sequence used to probe the interaction, as well as the subsequent multi-state detection step. Here, we use the convention φ_i , where φ and i are the rotation angle and axis, respectively, to specify the microwave pulse. Solid lines are theory curves from a full quantum mechanical

simulation of the dipolar interaction and molecule motion, with temperature and motion parameters determined from separate single-molecule measurements (Fig. 3), and tweezer separation and single-molecule dephasing chosen to match the data. **b**, Scaling of the interaction strength J as function of distance, with the black line representing a single-parameter fit with the function a/R^3 with best-fit value $a = 5.14(4) \text{ kHz } \mu\text{m}^{-3}$. Error bars in general represent 1σ confidence intervals, unless stated otherwise. **c**, Populations of the components of the Bell state created at an interaction time of $664 \mu\text{s}$, indicated by a dashed line in **a**. 1,282 trials are sampled. **d**, Parity oscillation signal $\Pi = P_{00} + P_{ee} - P_{0e} - P_{e0}$ after applying an additional global microwave $\pi/2$ -pulse with a variable phase to the Bell state (103 trials per point on average).

an additional global analysis microwave pulse with a variable phase to the pair of molecules and measuring the parity of the resulting two-qubit state (Methods). The total entanglement fidelity is determined by the coherence and the diagonal populations. Figure 2d shows this measured parity oscillation signal, along with the populations of all the two-molecule states before the analysis pulse in Fig. 2c. We extract a coherence of $C = 0.93(3)$ using a weighted least squares fit, and populations $P_{00} = 0.47(1)$ and $P_{ee} = 0.48(1)$. The total entanglement fidelity, conditioned on the detection of both molecules at the end of the sequence, is thus $F = 0.94(3)$. This is consistent to within 1σ with a maximum fidelity of 0.97 predicted given the currently observed decoherence of the dipole–dipole interaction.

Motion–rotation coupling

The noise on the interaction strength that limits the entanglement fidelity can be induced by the relative motion of the molecules, which leads to fluctuation of R and θ in equation (1). We first focus on the rotational coherence between $|0\rangle$ and $|e\rangle$ of a single molecule in a tweezer. A common way to remove noise and extend single-particle coherence is to apply dynamical decoupling^{10–13}. However, if we decouple this noise by choosing the pulse separation $\tau_{\text{XY-S}} \ll |\hbar/2J|$ we empirically find that

coherence is reduced. There is a prominent dip for $\tau_{\text{XY-S}}$ close to π/ω_{ax} , changing with trap depth, caused by parametric heating (Fig. 3a). Taking into account finite pulse widths and a realistic trap model (Methods), we extract an axial trap frequency of $4.95(1) \text{ kHz}$ for the trap used in the previous section from a fine scan of $\tau_{\text{XY-S}}$.

Parametric heating occurs if rotational states are coupled to motion. We construct a minimal coupling model with a state-dependent displacement of the trapping potential as shown in Fig. 3b described by

$$\hat{H}_{\text{motion-rotation}} = \hbar\omega_{\text{ax}}\hat{a}^\dagger\hat{a} - \frac{\hbar\zeta\omega_{\text{ax}}}{2}|e\rangle\langle e|(\hat{a} + \hat{a}^\dagger), \quad (2)$$

and attribute the origin of the coupling to optical aberrations, specifically astigmatism. Here, ζ is the displacement in units of harmonic oscillator length $\sqrt{\hbar/(2m\omega_{\text{ax}})} = 80 \text{ nm}$, with $m = 156$ atomic mass units the mass of NaCs and ω_{ax} the axial trapping frequency, and \hat{a} is the lowering operator of the axial trap in the harmonic approximation.

We now introduce a new method to measure both ζ and the temperature of the molecules by using this coupling to transfer motional excitation to internal rotational states, motivated by similar techniques for ions⁴³. In a spin-echo Ramsey experiment (Fig. 3c, inset), motion will lead to coherent dephasing and rephasing with half the trap frequency,

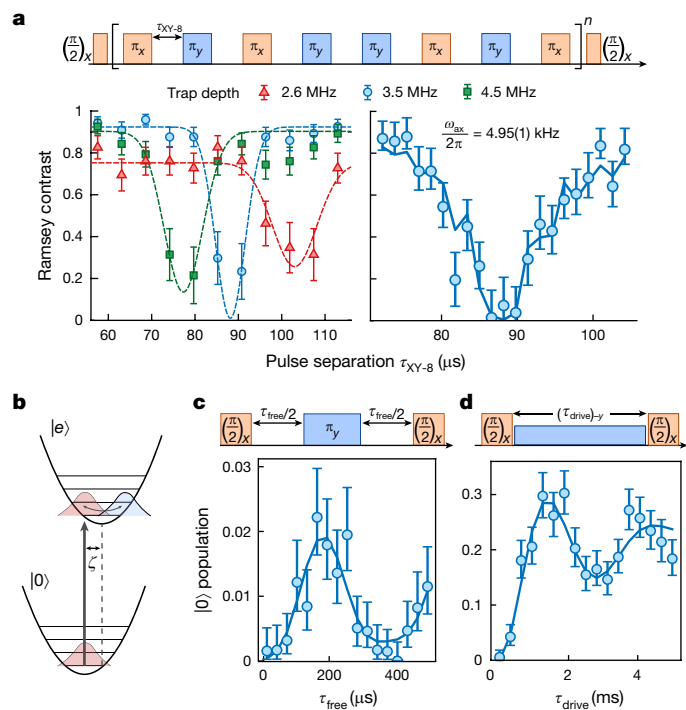


Fig. 3 | Coherent motion-rotation coupling to characterize molecule temperature and trap displacement ζ . **a**, Measured Ramsey coherence as a function of pulse separation τ_{XY-8} between XY-8 π -pulses. The left plot shows three different trap depths (inferred from theoretical polarizability of NaCs; refs. 11,59), at which we apply three XY-8 repetitions, totalling 24 π -pulses. By altering the tweezer depth during the measurement, we can modify the trapping frequency ω_{ax} , which shifts the τ_{XY-8} that produces maximal decoherence. Dashed lines are a Gaussian fit serving as a guide to the eye. The right plot shows a detailed spectrum of the noise peak at the depth of 3.5 MHz, the depth used for dipolar interactions data in Fig. 2. From this spectrum, which is probed with six XY-8 repetitions, we extract an axial trap frequency of 4.95(1) kHz. **b**, Illustration of the motional wavefunction of a single molecule following excitation from $|0\rangle$ to $|e\rangle$ when the $|e\rangle$ trapping potential is displaced. **c**, Observed oscillations in $|0\rangle$ at the axial trapping frequency as a function of free evolution time τ_{free} , during a spin-echo sequence. We postselect an average of 617 trials per point in which at least one molecule is detected. **d**, Population in $|0\rangle$ under continuous microwave drive along the $-y$ direction, where the drive Rabi frequency of $\Omega/2\pi = 5.18(3)$ kHz is chosen to be close to the axial trapping frequency. An average of 153 trials are per point are sampled. The solid lines in **a**, **c** and **d** are generated by the same theoretical model with temperature, trap displacement and dephasing parameters chosen to match all of the data simultaneously.

as the spatial wavepackets of the two internal states $|0\rangle$ and $|e\rangle$ separate and recombine. This measurement is sensitive to a combination of the trap frequency and temperature of the molecules⁴⁴ (Methods).

We can couple motion and rotation more directly by applying a continuous resonant drive with a Rabi frequency $\Omega = \omega_{ax}$, which generates dressed rotational states $|\pm\rangle = (|0\rangle \pm |e\rangle)/\sqrt{2}$ with an energy separation $\hbar\Omega$. In the dressed state picture, the motion-rotation coupling in equation (2) enables resonant excitation transfer between motion and rotation driven by $\hat{H}_{eff} = \zeta\omega_{ax}/4(|+\rangle\langle -| + |-\rangle\langle +| + |\hat{a}^\dagger|)$, where rotating terms at frequency ω_{ax} have been neglected. We prepare the initial state as the lower dressed state $|-\rangle$ by applying a $\pi/2$ -pulse with a phase $+90^\circ$ with respect to the drive. A final $\pi/2$ -pulse with the same phase maps the dressed states back to the $|0\rangle$, $|e\rangle$ basis for readout. Because this transfer from the $|-\rangle$ state occurs only if initial motional excitation is present, the oscillation amplitude is directly related to the motional ground state fraction. We perform this experiment using a Rabi frequency of $\Omega/2\pi = 5.18(3)$ kHz, slightly detuned from ω_{ax} , resulting in

oscillation at the generalized motion-dependent Rabi frequency $\sqrt{\hat{a}^\dagger \hat{a} \zeta^2 \omega_{ax}^2/4 + (\Omega - \omega_{ax})^2}$ with decreased amplitude.

To fit the data, we use a discrete variable representation to model the trap generated by a tweezer with astigmatism, producing a displacement ζ , from first principles. We find $\hbar\omega_{ax}/(k_B T) = 0.42(6)$ corresponding to an axial ground state fraction of 34(4)% and $\zeta = 0.062(5)$ from an astigmatism of 0.13(1) λ , with errors estimated using parametric bootstrapping (Methods). This ground state fraction is consistent with a previously measured lower bound on the molecule temperature using thermometry of atoms after dissociation³⁷ but is lower than expected given the measured Feshbach molecule production efficiency under the assumption of identical trapping frequencies for both atoms.

With these parameters, we can use the discrete variable representation to model the two-molecule contrast oscillations in Fig. 2a (see Methods for details). We include single-molecule decoherence with a decoherence time of 80 ms to match the rise of $|e0\rangle$ and $|0e\rangle$ population and set the distance to 1.79 μm to match the observed oscillation frequency. We find good quantitative agreement between theory and data. We use our model to compute a Bell state infidelity of 3(1)%, consistent with the measurement, with a contribution of around 1% because of single-molecule dephasing, and the rest because of finite temperature and astigmatism (Extended Data Fig. 2).

Looking ahead, without single-molecule dephasing and assuming a ground state fraction of 80%, our model predicts a Bell state infidelity of 0.4% limited by aberrations. Finally, by eliminating astigmatism, which could be achieved through in situ optimization of the tweezer wavefront using a spatial light modulator⁴⁵, the infidelity could be decreased to 2×10^{-4} . This remaining infidelity contains approximately equal contributions from residual thermal motion and interaction back action onto motion⁴⁶. This back action comes from the mechanical force that the dipoles exert on each other, which even at zero temperature can lead to off-resonant population transfer to motionally excited states. This effect can ultimately be reduced by increasing tweezer separation or confinement, to either reduce the force, which goes as $1/R^4$, or make population transfer more off-resonant.

Quantum logic gates between hyperfine qubits

The dipolar exchange interaction can naturally realize an iSWAP gate, which is a universal two-qubit gate, when the duration of the interaction is precisely controlled⁴. The Bell state creation protocol demonstrated thus far limited the duration of the interaction using global pulses applied to a particular initial state. To realize an iSWAP gate for any arbitrary input within the computational basis that can be applied multiple times, we need to switch the dipolar interactions on and off and show the desired logic outcomes.

Here, we introduce a third state, $|1\rangle$ (Fig. 1b), within the ground rotational manifold, which we use to implement the iSWAP gate with a qubit that does not natively interact⁴. The qubit is encoded in a hyperfine degree of freedom, which is insensitive to external fields and can maintain long coherence times⁶⁻⁸. The state $|1\rangle$ is weakly coupled to $|e\rangle$ by the nuclear quadrupole moment⁴⁷ and is chosen among all the accessible hyperfine states because it is the most detuned from $|0\rangle$, allowing for easier individual manipulation. The interaction is toggled by transferring between $|1\rangle$ and the rotationally excited state $|e\rangle$.

We engineer the interaction between qubits using the pulse sequence shown in Fig. 4a. We initialize a pair of molecules in the computational basis at a 5 μm trap separation with site-selective $|0\rangle$ to $|e\rangle$ transfer³⁷ and a 310 μs π -pulse from $|e\rangle$ to $|1\rangle$ (Extended Data Fig. 3). At 1.9 μm trap separation, we toggle the interaction with the same hyperfine state changing π -pulse ($|1\rangle \leftrightarrow |e\rangle$), and apply a spin-echo pulse on the $|0\rangle \leftrightarrow |e\rangle$ transition in the middle of the interaction period.

For detection, we transfer $|1\rangle$ to $|e\rangle$ at a 5 μm trap separation and read out the $|0\rangle$ and $|e\rangle$ states. Figure 4b shows the dipolar interaction between two qubits initialized in the $|01\rangle$ state. Here, the post-selection

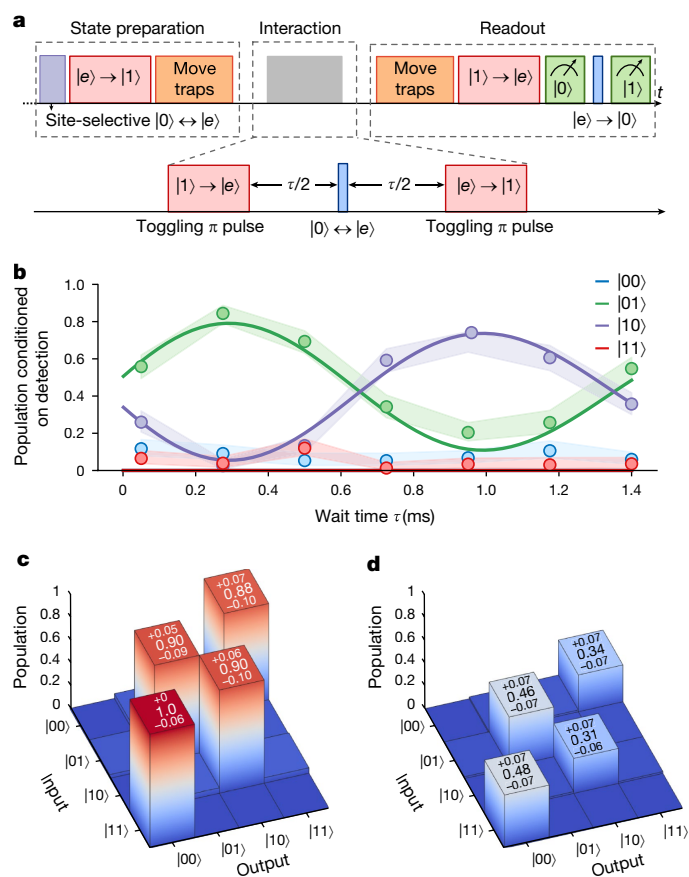


Fig. 4 | Engineering dipolar interaction and the iSWAP gate between hyperfine-state-encoded qubits. **a**, Microwave pulse sequence for implementing an iSWAP gate between two hyperfine qubits. **b**, Time evolution of resonant dipolar exchange for a pair of molecules initially prepared in the two-qubit state $|01\rangle$. We postselect an average of 78 trials per point in which both molecules are detected in the computational $|0\rangle$, $|1\rangle$ basis. Solid lines are theory curves from a master equation model, using parameters extracted from the data in Fig. 2. **c**, Measured truth tables for the full iSWAP gate sequence, showing the probabilities of measuring each two-qubit output state given each input state, conditioned on detection of two molecules in the $(|0\rangle, |1\rangle)$ manifold (average of 29 trials per point). This represents the truth table for the entangling interaction with leakage errors caused by the single-qubit gate removed. **d**, iSWAP truth table showing the probabilities relative to the probability of detecting the $|00\rangle$ state with no pulses applied. Losses here are dominated by leakage to the $|e\rangle$ state because of imperfect hyperfine state changing pulses both during state preparation and measurement and in the toggling pulses that start and end the gate.

of the data is done for trials in which a pair of molecules are both detected within the qubit subspace. The exchange interaction leads to oscillation between the $|01\rangle$ and $|10\rangle$ states. The full exchange occurs $330 \mu\text{s}$ after the end of the toggling pulse, shorter than if the pulses were infinitely fast because the interaction occurs already during the duration of the toggling pulse.

At the full exchange time, the sequence realizes the iSWAP gate up to a global rotation, originating from the spin-echo pulse. The total gate time, composed of the full exchange time and the duration of both toggling pulses, is $960 \mu\text{s}$. The unitary corresponding to the ideal implementation in the $(|0\rangle, |1\rangle)$ basis is

$$U = \begin{bmatrix} 0 & 0 & 0 & -1 \\ 0 & -i & 0 & 0 \\ 0 & 0 & -i & 0 \\ -1 & 0 & 0 & 0 \end{bmatrix}. \quad (3)$$

Under the application of this gate, $|01\rangle$ and $|10\rangle$ obtain a non-trivial phase of $-i$ from the dipolar exchange, which is the same phase we verified using the parity oscillation of the Bell state in Fig. 2c. We characterize the logic outcomes of the iSWAP gate for each computational basis state and show the resulting population truth table in Fig. 4c (see Extended Data Fig. 4 for details). For trials in which two molecules are detected in the qubit subspace, an average of the probabilities for each input state to transform into the intended output state yields a truth table fidelity⁴⁸ of $0.92^{+0.05}_{-0.09}$.

The ease of choosing three states $|0\rangle$, $|1\rangle$ and $|e\rangle$ showcases the versatile structure of molecules, but the dense structure also risks causing leakage outside the computational basis⁴. To take leakage into account, we instead normalize the detected outcomes to the population measured in the initial state $|00\rangle$ before performing site-selective state preparation and the iSWAP gate. The corresponding truth table is shown in Fig. 4d and the resulting truth table fidelity is $0.39^{+0.1}_{-0.09}$.

The current gate fidelity is primarily limited by leakage during four hyperfine-changing pulses, which are needed for state preparation, the iSWAP gate and readout. Rotational transitions that change nuclear spin are two orders of magnitude weaker than those that conserve nuclear spin at a magnetic field of 864 G. The strong microwave pulse required to drive the hyperfine-changing transition introduces off-resonant Stark shifts from nearby transitions making the transfer pulse sensitive to microwave amplitude noise. The Stark shifts specifically from non-magic rotational states fluctuate with trap intensity noise and further decohere the transition. Owing to these decoherence sources, the current one-way transfer efficiency is limited to 89%. The hyperfine-changing transfer could be made more coherent with active microwave amplitude stabilization and polarization control. The latter also mitigates depopulation of the $|0\rangle$ state, allowing faster driving of the transition. Another source of leakage is because of interactions during the toggling pulses. We anticipate that 9% of population leaves the computational basis with perfect hyperfine-changing transfer at the current toggling duration. This leakage would decrease quadratically with increased pulse duration or could be mitigated using a different transfer scheme, such as detuned microwave or optical Raman transfer. Both leakage sources described here lead to populations remaining in $|e\rangle$ and the state $|e'\rangle$ with the same nuclear spin quantum numbers as $|1\rangle$, the latter occurring because of the spin-echo pulse (Methods). In the future, these populations could be detected without disturbing the computational basis by state-selective transfer to the $N = 2$ rotational states for readout. These detectable errors may be correctable using erasure conversion schemes^{49,50}.

Conclusions and outlook

We demonstrate a molecular iSWAP gate, a key requirement for universal quantum computation with polar molecules. The gate is based on the native coherent interaction between molecules, such that noise on the interaction is more because of imperfect state preparation than to variations in external fields. We characterize the interaction by measuring a two-molecule Bell state entanglement fidelity of 94(3)% with error primarily due to imperfect motional state preparation (34(4)% axial ground state fraction). A modest improvement in the axial ground state fraction to 80% and elimination of tweezer astigmatism and single-particle dephasing would yield a fidelity exceeding 99.9%, at which point more fundamental decoherence mechanisms dominate. The iSWAP gate is mainly limited by imperfect transfer between hyperfine states because of the density of nearby molecular states with strong transitions that can induce a.c. Stark shifts and population leakage. This could be improved through finer microwave polarization and amplitude control, opening up the complex molecular structure for multi-level applications. Excitations to multiple rotational levels, paired with coherent dipolar interactions, will enable quantum simulation of complex many-body Hamiltonians^{51,52} and encoding of robust logical

qubits²⁶ and qudits²⁷. In parallel, efforts to pursue efficient molecule production and detection remain important for the utility of the molecular platform, for example, in a hybrid molecule Rydberg system with orders of magnitude faster gates and mid-circuit readout of molecular states^{53–55}. The coherent control of motion–rotation coupling offers a new sensitive probe of molecular temperature and confinement, adding another degree of freedom to the molecule toolbox. This promises new opportunities for quantum simulation and metrology based on spin-motion entanglement^{43,56–58}.

Online content

Any methods, additional references, Nature Portfolio reporting summaries, source data, extended data, supplementary information, acknowledgements, peer review information; details of author contributions and competing interests; and statements of data and code availability are available at <https://doi.org/10.1038/s41586-024-08177-3>.

- DeMille, D. Quantum computation with trapped polar molecules. *Phys. Rev. Lett.* **88**, 067901 (2002).
- Yelin, S. F., Kirby, K. & Côté, R. Schemes for robust quantum computation with polar molecules. *Phys. Rev. A* **74**, 050301 (2006).
- Zhu, J., Kais, S., Wei, Q., Herschbach, D. & Friedrich, B. Implementation of quantum logic gates using polar molecules in pendular states. *J. Chem. Phys.* **138**, 024104 (2013).
- Ni, K.-K., Rosenband, T. & Grimes, D. D. Dipolar exchange quantum logic gate with polar molecules. *Chem. Sci.* **9**, 6830–6838 (2018).
- Hudson, E. R. & Campbell, W. C. Dipolar quantum logic for freely rotating trapped molecular ions. *Phys. Rev. A* **98**, 040302 (2018).
- Park, J. W., Yan, Z. Z., Loh, H., Will, S. A. & Zwiernik, M. W. Second-scale nuclear spin coherence time of ultracold ²³Na⁴⁰K molecules. *Science* **357**, 372–375 (2017).
- Gregory, P. D., Blackmore, J. A., Bromley, S. L., Hutson, J. M. & Cornish, S. L. Robust storage qubits in ultracold polar molecules. *Nat. Phys.* **17**, 1149–1153 (2021).
- Lin, J., He, J., Jin, M., Chen, G. & Wang, D. Seconds-scale coherence on nuclear spin transitions of ultracold polar molecules in 3d optical lattices. *Phys. Rev. Lett.* **128**, 223201 (2022).
- Burchesky, S. et al. Rotational coherence times of polar molecules in optical tweezers. *Phys. Rev. Lett.* **127**, 123202 (2021).
- Christakis, L. et al. Probing site-resolved correlations in a spin system of ultracold molecules. *Nature* **614**, 64–69 (2023).
- Park, A. J. et al. Extended rotational coherence of polar molecules in an elliptically polarized trap. *Phys. Rev. Lett.* **131**, 183401 (2023).
- Holland, C. M., Lu, Y. & Cheuk, L. W. On-demand entanglement of molecules in a reconfigurable optical tweezer array. *Science* **382**, 1143–1147 (2023).
- Bao, Y. et al. Dipolar spin-exchange and entanglement between molecules in an optical tweezer array. *Science* **382**, 1138–1143 (2023).
- Lloyd, S. A potentially realizable quantum computer. *Science* **261**, 1569–1571 (1993).
- Gershenfeld, N. A. & Chuang, I. L. Bulk spin-resonance quantum computation. *Science* **275**, 350–356 (1997).
- Jones, J. A. & Mosca, M. Implementation of a quantum algorithm on a nuclear magnetic resonance quantum computer. *J. Chem. Phys.* **109**, 1648–1653 (1998).
- Vandersypen, L. M. K. et al. Experimental realization of Shor's quantum factoring algorithm using nuclear magnetic resonance. *Nature* **414**, 883–887 (2001).
- Menicucci, N. C. & Caves, C. M. Local realistic model for the dynamics of bulk-ensemble NMR information processing. *Phys. Rev. Lett.* **88**, 167901 (2002).
- Monroe, C. & Kim, J. Scaling the ion trap quantum processor. *Science* **339**, 1164–1169 (2013).
- Bluvstein, D. et al. Logical quantum processor based on reconfigurable atom arrays. *Nature* **626**, 58–65 (2024).
- Kjaergaard, M. et al. Superconducting qubits: current state of play. *Annu. Rev. Condens. Matter Phys.* **11**, 369–395 (2020).
- ACME Collaboration Improved limit on the electric dipole moment of the electron. *Nature* **562**, 355–360 (2018).
- Roussy, T. S. et al. An improved bound on the electron's electric dipole moment. *Science* **381**, 46–50 (2023).
- Micheli, A., Brennen, G. & Zoller, P. A toolbox for lattice-spin models with polar molecules. *Nat. Phys.* **2**, 341–347 (2006).
- Gorshkov, A. V. et al. Tunable superfluidity and quantum magnetism with ultracold polar molecules. *Phys. Rev. Lett.* **107**, 115301 (2011).
- Albert, V. V., Covey, J. P. & Preskill, J. Robust encoding of a qubit in a molecule. *Phys. Rev. X* **10**, 031050 (2020).
- Sawant, R. et al. Ultracold polar molecules as qudits. *New J. Phys.* **22**, 013027 (2020).
- Ni, K.-K. et al. A high phase-space-density gas of polar molecules. *Science* **322**, 231–235 (2008).
- Danzl, J. G. et al. Quantum gas of deeply bound ground state molecules. *Science* **321**, 1062–1066 (2008).
- Lang, F., Winkler, K., Strauss, C., Grimm, R. & Hecker Denschlag, J. Ultracold triplet molecules in the rovibrational ground state. *Phys. Rev. Lett.* **101**, 133005 (2008).
- Anderegg, L. et al. An optical tweezer array of ultracold molecules. *Science* **365**, 1156–1158 (2019).
- Cairncross, W. B. et al. Assembly of a rovibrational ground state molecule in an optical tweezer. *Phys. Rev. Lett.* **126**, 123402 (2021).
- Rosenberg, J. S., Christakis, L., Guardado-Sanchez, E., Yan, Z. Z. & Bakr, W. S. Observation of the Hanbury Brown–Twiss effect with ultracold molecules. *Nat. Phys.* **18**, 1062–1066 (2022).
- Ruttley, D. K. et al. Formation of ultracold molecules by merging optical tweezers. *Phys. Rev. Lett.* **130**, 223401 (2023).
- Zhang, J. T. et al. An optical tweezer array of ground-state polar molecules. *Quantum Sci. Technol.* **7**, 035006 (2022).
- Rosenband, T., Grimes, D. D. & Ni, K.-K. Elliptical polarization for molecular Stark shift compensation in deep optical traps. *Opt. Express* **26**, 19821–19825 (2018).
- Picard, L. R. B., Patenotte, G. E., Park, A. J., Gebretsadkan, S. F. & Ni, K.-K. Site-selective preparation and multistate readout of molecules in optical tweezers. *PRX Quantum* **5**, 020344 (2024).
- Aymar, M. & Dulieu, O. Calculation of accurate permanent dipole moments of the lowest ¹Σ⁺ states of heteronuclear alkali dimers using extended basis sets. *J. Chem. Phys.* **122**, 204302 (2005).
- Yan, B. et al. Observation of dipolar spin-exchange interactions with lattice-confined polar molecules. *Nature* **501**, 521–525 (2013).
- Wall, M. L., Hazzard, K. R. A. & Rey, A. M. In *From Atomic to Mesoscale: The Role of Quantum Coherence in Systems of Various Complexities* (eds Novikova, I. & Malinovsky, S. A.) 3–38 (World Scientific, 2015).
- Souza, A. M., Álvarez, G. A. & Suter, D. Robust dynamical decoupling. *Philos. Trans. R. Soc. A Math. Phys. Eng. Sci.* **370**, 4748–4769 (2012).
- Chomaz, L. et al. Dipolar physics: a review of experiments with magnetic quantum gases. *Rep. Prog. Phys.* **86**, 026401 (2023).
- Gilmore, K. A. et al. Quantum-enhanced sensing of displacements and electric fields with two-dimensional trapped-ion crystals. *Science* **373**, 673–678 (2021).
- Koller, A. P., Mundinger, J., Wall, M. L. & Rey, A. M. Demagnetization dynamics of noninteracting trapped fermions. *Phys. Rev. A* **92**, 033608 (2015).
- Chew, Y. T. et al. Ultra-precise holographic optical tweezers array. Preprint at <https://arxiv.org/abs/2407.20699> (2024).
- Chew, Y. et al. Ultrafast energy exchange between two single Rydberg atoms on a nanosecond timescale. *Nat. Photon.* **16**, 724–729 (2022).
- Aldegunde, J. & Hutson, J. M. Hyperfine structure of alkali-metal diatomic molecules. *Phys. Rev. A* **96**, 042506 (2017).
- Hofmann, H. F. Complementary classical fidelities as an efficient criterion for the evaluation of experimentally realized quantum operations. *Phys. Rev. Lett.* **94**, 160504 (2005).
- Ma, S. et al. High-fidelity gates and mid-circuit erasure conversion in an atomic qubit. *Nature* **622**, 279–284 (2023).
- Scholl, P. et al. Erasure conversion in a high-fidelity Rydberg quantum simulator. *Nature* **622**, 273–278 (2023).
- Sundar, B., Gadway, B. & Hazzard, K. R. A. Synthetic dimensions in ultracold polar molecules. *Sci. Rep.* **8**, 3422 (2018).
- Homeier, L. et al. Antiferromagnetic bosonic t–J models and their quantum simulation in tweezer arrays. *Phys. Rev. Lett.* **132**, 230401 (2024).
- Kuznetsova, E., Rittenhouse, S. T., Sadeghpour, H. R. & Yelin, S. F. Rydberg-atom-mediated nondestructive readout of collective rotational states in polar-molecule arrays. *Phys. Rev. A* **94**, 032325 (2016).
- Wang, K., Williams, C. P., Picard, L. R. B., Yao, N. Y. & Ni, K.-K. Enriching the quantum toolbox of ultracold molecules with Rydberg atoms. *PRX Quantum* **3**, 030339 (2022).
- Guttridge, A. et al. Observation of Rydberg blockade due to the charge-dipole interaction between an atom and a polar molecule. *Phys. Rev. Lett.* **131**, 013401 (2023).
- Guardado-Sanchez, E. et al. Quench dynamics of a Fermi gas with strong nonlocal interactions. *Phys. Rev. X* **11**, 021036 (2021).
- Carroll, A. N. et al. Observation of generalized t–J spin dynamics with tunable dipolar interactions. Preprint at arxiv.org/abs/2404.18916 (2024).
- Shaw, A. L. et al. Erasure-cooling, control, and hyper-entanglement of motion in optical tweezers. Preprint at arxiv.org/abs/2311.15580 (2023).
- Vexiau, R. et al. Dynamic dipole polarizabilities of heteronuclear alkali dimers: optical response, trapping and control of ultracold molecules. *Int. Rev. Phys. Chem.* **36**, 709–750 (2017).

Publisher's note Springer Nature remains neutral with regard to jurisdictional claims in published maps and institutional affiliations.

Springer Nature or its licensor (e.g. a society or other partner) holds exclusive rights to this article under a publishing agreement with the author(s) or other rightsholder(s); author self-archiving of the accepted manuscript version of this article is solely governed by the terms of such publishing agreement and applicable law.

© The Author(s), under exclusive licence to Springer Nature Limited 2024

Methods

External fields and quantization

We define the quantization axis to be along the magnetic field of 863.9 G, which is kept constant during the experiment and is parallel to the k -vector of the optical tweezer. The large magnetic field independently aligns the nuclear spins of the two atoms and decouples them from molecular rotation. At the trap depths we use, the rotational sublevels are split by hundreds of kHz by the a.c. electric field of the optical tweezer¹¹, which is elliptically polarized in the plane perpendicular to the quantization axis. We label three states relevant to this work: the state in which assembled molecules are initially prepared, $|0\rangle \equiv |N=0, m_N=0, m_{I_{\text{Na}}}=3/2, m_{I_{\text{Cs}}}=5/2\rangle$ (ref. 32); the magic state in the first rotationally excited manifold with the same nuclear hyperfine quantum numbers, $|e\rangle \equiv |N=1, m_{I_{\text{Na}}}=3/2, m_{I_{\text{Cs}}}=5/2\rangle \otimes \frac{1}{\sqrt{2}}(|m_N=1\rangle - |m_N=-1\rangle)$ (ref. 11); and an additional nuclear hyperfine state in the rotational ground manifold that we use as one of our qubit states, $|1\rangle \equiv |N=0, m_N=0, m_{I_{\text{Na}}}=-1/2, m_{I_{\text{Cs}}}=5/2\rangle$. The particular decomposition of $|e\rangle$ in terms of rotational sublevels is determined by the orientation of the tweezer polarization ellipse, which we choose to have its minor axis parallel to the intermolecular axis.

Molecule preparation and detection

The procedure for preparing single ultracold NaCs molecules in optical tweezers is detailed in our previous work^{32,35,60,61}. Briefly, we begin by Raman sideband cooling Na and Cs atoms in separate optical tweezer arrays. We then merge the arrays, perform magnetoassociation of the atoms into molecules at a Feshbach resonance, and perform a two-photon detuned Raman transfer to the rovibrational ground state. Specifically, we prepare the molecules in the $|0\rangle$ state, which has the largest coupling to the weakly bound Feshbach molecule given our choice of σ^+ polarization for both the Pump and Stokes lasers used in two-photon transfer.

After preparing the molecules in an eight-site array, we detect and remove any remaining unassociated Cs atoms and rearrange the molecules to a higher density region at one end of the array. All dipole-dipole interaction data reported in this work includes only the two sites with the highest molecule density at the end of the array. To detect the molecule population, we transfer from $|0\rangle$ back to the weakly bound Feshbach molecule, perform magnetodissociation at the Feshbach resonance, and image the resultant Cs atoms. As the two-photon transfer is far off-resonant for the $|e\rangle$ state, we can perform this process sequentially: first measuring $|0\rangle$ in one image and then transferring the remaining population from $|e\rangle$ to $|0\rangle$ before repeating the process. This allows us to read out both $|0\rangle$ and $|e\rangle$ in each shot of the experiment. To initially prepare a pair of molecules in different internal state combinations starting from the $|00\rangle$ state, we use site-selective excitation of molecules using dynamic ramping of tweezer depths combined with microwave shelving pulses, as detailed in ref. 37.

Microwave pulse sequences

To probe dipole-dipole interactions between $|0\rangle$ and $|e\rangle$, we begin with a pair of molecules in the $|00\rangle$ state and apply a $\pi/2$ -pulse to prepare the product state $\frac{1}{\sqrt{2}}(|0\rangle - |e\rangle) \otimes \frac{1}{\sqrt{2}}(|0\rangle - |e\rangle)$. The phase of this first pulse defines rotation about the x -axis of the Bloch sphere. We then allow the system to evolve under H_{DD} for time τ before applying another $\pi/2$ -pulse. To cancel out any phase accumulation due to finite detuning of the microwave pulse from resonance or slow drifts in the resonance frequency, we apply a spin-echo π -pulse in the middle of the interaction period, with a phase of $+90^\circ$ relative to the initial pulse, realizing an effective y -rotation. This sequence is shown in Fig. 2 (inset). The π -pulses have a total duration of 12.83 μs , and for all pulses addressing this transition, we use a truncated Gaussian pulse shape with a width 0.3 times the pulse duration to reduce off-resonant coupling to other rotational states⁶².

To investigate the impact of molecule motion, we perform noise spectroscopy using dynamical decoupling. At a large molecule separation, in which there is no substantial dipole-dipole interaction on relevant timescales, we perform a Ramsey sequence composed of a $\pi/2$ -pulse on $|0\rangle \leftrightarrow |e\rangle$, a series of dynamical decoupling pulses, and a final $\pi/2$ -pulse for readout. We use the XY-8 decoupling pulse sequence, consisting of evenly spaced π -pulses along the x - and y -axes, shown in Fig. 3a, which cancels the effect of any pulse area imperfections⁴¹. To observe coherent effects of motional dephasing and rephasing, we use the same spin-echo pulse sequence as described above, as well as a continuous drive sequence, described in full in the main text.

We probe the strength of the motion-rotation coupling using a spin-echo Ramsey sequence, in which the population in $|0\rangle$ oscillates at the axial trapping frequency, as shown in Fig. 3c. In the harmonic approximation, the functional form of the oscillation is given by $1 - \exp\left(\frac{-2\zeta^2 \sin^4(\omega_{\text{ax}} t/4)}{\tanh[\hbar\omega_{\text{ax}}/(2k_{\text{B}}T)]}\right)$ (ref. 44). As a consequence, this measurement is sensitive to the joint parameter $\zeta^2/\tanh[\hbar\omega_{\text{ax}}/(k_{\text{B}}T)]$, where T is the molecule temperature and k_{B} is the Boltzmann constant.

To perform an iSWAP gate between hyperfine qubits, we toggle the interaction on and off using 310 μs square π -pulses on the $|1\rangle \leftrightarrow |e\rangle$ transition. At the midpoint of the interaction period, we apply a single spin-echo π -pulse on $|0\rangle \leftrightarrow |e\rangle$ with a duration of 12.83 μs and a truncated Gaussian shape, as before.

Hyperfine spectroscopy

To identify a suitable hyperfine state to act as the $|1\rangle$ state of the hyperfine storage qubit, we spectroscopically investigate multiple nuclear-spin-changing transitions from $|e\rangle$. Transitions that change nuclear spin are mediated by the electric quadrupole interaction⁴⁷ and are significantly weaker than those which do not. The state $|1\rangle$ was chosen because it is the state furthest detuned from $|0\rangle$, which still has significant coupling to $|e\rangle$, such that off-resonant coupling to $|e'\rangle$, an excited rotational state of the same hyperfine manifold as $|1\rangle$, is suppressed. The full hyperfine structure of NaCs is shown in Extended Data Fig. 5, along with a simulated spectrum of the couplings of the $|1\rangle$ and $|e\rangle$ states under a strong microwave drive.

Post-selection and error analysis

To study the interactions between molecules, we post-select on cases in which two molecules are detected at the readout stage, which is enabled by the fact that we measure both $|0\rangle$ and $|e\rangle$ during each experimental run. Post-selection enables us to eliminate background in the interaction signal due to shots in which one or both traps are empty, at the expense of discarding shots in which both molecules were present but one or both were not detected because of measurement error. The only remaining background on the signal obtained by post-selection is because of the small 0.0038 false-positive rate of the imaging step, giving a negligible contribution of 10^{-5} to the two-body signal (assuming uncorrelated false positives between sites)³⁷. The outcomes of each trial following post-selection are described by a binomial distribution,

$$p(S|X, N_{\text{Trial}}) = \binom{N_{\text{Trial}}}{S} X^S (1-X)^{N_{\text{Trial}}-S},$$

where the number of binomial trials, N_{Trial} , is the total number of molecules detected and the number of binomial successes, S , is the number detected in a particular state combination with a corresponding population X . Given a measurement of S , the maximum likelihood estimator of the population, \hat{X} , and associated 1σ confidence interval can be computed by inverting the distribution using the Clopper-Pearson method⁶³.

Entanglement fidelity

To measure the fidelity with which we prepare a Bell state, we apply a $\pi/2$ -pulse with a variable phase to the state and measure the

Article

parity-signal $\Pi = P_{00} + P_{ee} - P_{0e} - P_{e0}$. We expect this signal to oscillate with the applied phase ϕ as $\Pi = C \sin(2\phi)$, where the amplitude, C , of the parity oscillation is the coherence⁶⁴. The total entanglement fidelity is determined by the coherence and the diagonal populations of the components of the state, $F = \frac{1}{2}(C + P_{00} + P_{ee})$.

Master equation model of decoherence

We perform the initial analysis of the strength and decoherence of the dipole–dipole interaction using a Lindblad master equation with three phenomenological decay channels corresponding to dephasing of the dipole–dipole interaction itself, relative detuning noise between the two molecules and global detuning noise on both molecules. These processes are represented, respectively, by the jump operators:

$$L_J = \sqrt{\gamma_J}(|0e\rangle\langle e0| + |e0\rangle\langle 0e|), \quad (4)$$

$$L_\delta = \sqrt{\gamma_\delta}(|e0\rangle\langle e0| - |0e\rangle\langle 0e|), \quad (5)$$

$$L_\Delta = \sqrt{\gamma_\Delta}(|ee\rangle\langle ee| - |00\rangle\langle 00|). \quad (6)$$

We fit the master equation model to the data by minimizing the weighted least squares residual of the model and experimental data, using the Nelder–Mead algorithm to optimize the rates of the decoherence processes along with the interaction strength, J , and a static relative detuning, δ , between the molecules. We implement the master equation model using the Julia Quantum Optics toolbox⁶⁵.

Numerical simulations of motion

To simulate the dynamics with motion–rotation coupling, we use a combination of discrete variable representation (DVR) and exact diagonalization. We compute the local electromagnetic field of a single tweezer in the presence of astigmatism using vector Debye theory, specifically eq. (7) of ref. 66. The objective is modelled as a curved wavefront S from which plane waves with wavenumber κ are emitted in a direction orthogonal to the surface \mathbf{s} and interfere to produce the focus of an optical tweezer. The electric field \mathbf{E} at a point \mathbf{P} is defined by the Debye–Wolf integral

$$\mathbf{E}(\mathbf{P}) \propto \iint_S \frac{\mathbf{a}(s_x, s_y)}{s_z} \exp\{i\kappa[\Phi(s_x, s_y) + \mathbf{s} \cdot \mathbf{r}(\mathbf{P})]\} ds_x ds_y, \quad (7)$$

where \mathbf{a} is related to the laser polarization at each point on the wavefront, Φ is a distortion to the wavefront phase caused by an aberration, and \mathbf{r} is a vector between the objective and the point \mathbf{P} .

Of the primary aberrations, astigmatism and coma produce displacement of the $|0\rangle$ and $|e\rangle$ states in the axial and radial directions, respectively, by altering the ellipticity of the tweezer polarization at the focus. The distortion provided by astigmatism is defined to be

$$\Phi_a = A_a \rho^2 \cos^2(\phi), \quad (8)$$

where A_a is the amplitude of astigmatism in units of distance, and ρ and ϕ are polar coordinates in the objective plane that is orthogonal to the optical axis. We assume that the vertical axis of astigmatism ($\phi = 0$) is oriented along the probable distortion of the laser in the horizontal plane, parallel to the minor axis of the polarization ellipse.

The local energy $V_{0/e}(x, y, z)$ of the two states was determined from their polarizabilities α_0 and $\alpha_0 + \alpha_2 \frac{1 - 3 \cos(2\chi)}{10}$, where α_0 and α_2 are the theoretical scalar and tensor polarizabilities of NaCs in a 1,064-nm tweezer⁵⁹. We identify the position of minimal energy by gradient descent, which corresponds to the point of maximum intensity for $|0\rangle$.

We compute the potential energy $V_{0/e}(x, y, z)$ of both internal states on a grid centred around the $|0\rangle$ minimum with grid spacing $a_{\text{grid}} = 50$ nm and dimensions $17 \times 17 \times 37$, chosen to correspond

to a constant energy cutoff. Following ref. 67, we construct the single-molecule DVR Hamiltonian in second quantization for each potential energy surface as

$$\hat{H}_{\text{motion},\alpha} = \sum_{x,y,z} \left[\left(V_\alpha(x, y, z) + \frac{\pi^2 \hbar^2}{6ma_{\text{grid}}^2} \right) \hat{b}_{\alpha;x,y,z}^\dagger \hat{b}_{\alpha;x,y,z} + \sum_d \frac{\hbar^2 (-1)^d}{ma_{\text{grid}}^2 d^2} \hat{b}_{\alpha;x,y,z}^\dagger (\hat{b}_{\alpha;x+d,y,z} + \hat{b}_{\alpha;x,y+d,z} + \hat{b}_{\alpha;x,y,z+d}) \right] \quad (9)$$

Here, $\alpha = 0, e$ is the internal state and $\hat{b}_{\alpha;x,y,z}$ is the annihilation operator for a molecule in state α at position (x, y, z) and d runs over all integers for which the annihilation and creation operators outside the basis grid are set to zero.

We numerically compute the n lowest motional eigenenergies and corresponding eigenstates of each rotational state. We choose the tweezer depth to match the numerically extracted level spacing to the experimentally measured value of $\hbar \times 4.95$ kHz.

To compute the two-body Hamiltonian of dimension $4n^2$, we project the dipolar interactions described by the Hamiltonian

$$\hat{H}_{\text{dip}} = \frac{1}{2} \int d^3\mathbf{r} d^3\mathbf{r}' \frac{1 - 3\cos^2(\theta)}{4\pi\epsilon_0 |\mathbf{r} - \mathbf{r}'|^3} [\hat{\psi}_e^\dagger(\mathbf{r}) \hat{\psi}_0^\dagger(\mathbf{r}') \hat{\psi}_e(\mathbf{r}') \hat{\psi}_0(\mathbf{r}) + \text{h.c.}] \quad (10)$$

into the low-energy eigenstates, where we replace integrals with sums over discrete grid values. Here, θ is the angle between $\mathbf{r} - \mathbf{r}'$ and the electric field. Analogously, we also project the pulse or drive Hamiltonian

$$\hat{H}_{\text{pulse}} = \frac{\Omega}{2} |0\rangle\langle e| + \frac{\Omega^*}{2} |e\rangle\langle 0| + \Delta |e\rangle\langle e| \quad (11)$$

into the DVR basis, which couples different motional levels according to their state overlap. We choose Δ such that the microwave pulse is exactly in resonance $\Delta = -\langle \psi_0 | \hat{H}_{\text{motion},e} | \psi_0 \rangle + \langle \psi_0 | \hat{H}_{\text{motion},0} | \psi_0 \rangle$, where $|\psi_0\rangle$ is the ground state of $\hat{H}_{\text{motion},0}$. We numerically verify that residual detuning less than approximately $\hbar \times 1$ kHz is removed by spin-echo. It is important to simulate the spin-motion-coupled dynamics during the pulse evolution as the finite pulse width leads to shifts of the naively estimated trap frequency by approximately $\tau_{\text{pulse}}/\tau_{\text{XY-S}}$, that is, several percent.

Finally, we include single-molecule dephasing at rate γ_{deph} described by the Lindblad operators

$$\hat{L}_j = \sqrt{\frac{\gamma_{\text{deph}}}{2}} (|e\rangle\langle e|_j - |0\rangle\langle 0|_j). \quad (12)$$

For the single-molecule simulations, we further include motional dephasing modelled by the diagonal matrix

$$\hat{L}_{\text{motion},j} = \sqrt{2\gamma_{\text{motion}}} \begin{pmatrix} 1 & 0 & \dots & 0 \\ 0 & 2 & \dots & 0 \\ \vdots & \vdots & \ddots & \vdots \\ 0 & 0 & \dots & n \end{pmatrix}. \quad (13)$$

We then propagate the resulting master equation in real time to reproduce the experimental data. We ignore any dephasing that occurs during the pulses for simplicity, which is expected to be insignificant for pulse durations of about 10 μs , but keep dipolar interactions on during the pulses.

To make the two-particle simulations more efficient, we ignore off-diagonal elements between motional states whose energies differ by more than $\hbar \times 200$ Hz when computing the lines for Fig. 2. As the coupling between these manifolds due to dipolar interactions is less than about $\hbar \times 10$ Hz close to the ground state, this affects only dynamics

during pulses. It removes small oscillations with an amplitude of a few per cent, smaller than experimental error bars, from the theory curves.

In all simulations, we set $\Omega = h \times 38$ kHz, $\gamma_{\text{deph}} = 1/(80$ ms) and $R = 1.79$ μm , slightly smaller than the experimentally measured value, to match the observed interaction rate for a molecule-frame dipole moment $d = 4.6$ debye. We choose a temperature-dependent cutoff for the number of motional eigenstates included in the simulations. For the single-molecule simulations, we choose the cutoffs $n = 30$ [$0.6 \leq \hbar\omega_{\text{ax}}/(k_{\text{B}}T)$]; $n = 40$ [$0.4 \leq \hbar\omega_{\text{ax}}/(k_{\text{B}}T) < 0.6$]; $n = 50$ [$\hbar\omega_{\text{ax}}/(k_{\text{B}}T) < 0.4$]. For the two-molecule simulations for Fig. 2, we set $n = 30$. The DVR simulations were written in the Julia programming language⁶⁸ using the KrylovKit package⁶⁹.

Parametric bootstrapping for fit parameter uncertainty

To determine the best-fit parameters to match the data, we first fix the trap frequency using the XY-8 scan in Fig. 3a by generating simulated curves for a range of trap frequency values, computing the weighted squared residuals between the curve and the data for each point, and fitting a parabola to determine the best-fit trap frequency. To fit the remaining parameters to the XY-8, spin-echo and continuous drive data in Fig. 3 simultaneously, we generate curves for a three-dimensional grid of the temperature T , astigmatism and motional dephasing γ_{motion} parameters. We then approximate the best-fit value as the grid point that gives the lowest weighted squared residual for the combined data.

To estimate the uncertainties in the optimized parameters of the master equation and motion–rotation models, we apply the parametric bootstrap method⁷⁰. For every dataset which we fit, we generate new bootstrap samples using the estimator \hat{X} for each two-molecule state at each point, drawing from the distribution $p(S|\hat{X}, N_{\text{Trial}})$. We then repeat the fitting procedure for each bootstrapped sample, generating a distribution of optimal fit parameters. We generate 300 bootstrap samples for each experimental dataset for the master equation fit and 500 for the motion–rotation model. The uncertainties in the fit parameters represent the standard deviation of their distribution. In the case of the motion–rotation model, we also approximate the maximum likelihood estimators of the parameters as the mean of the bootstrapped samples.

Tweezer separation

We estimate the tweezer separation from the frequencies of the radio-frequency tones applied to the acousto-optic deflector used to generate the tweezers and the expected propagation of beams through a 4f optical system³⁵. This does not account for any systematic deviations of the tweezers from ideal Gaussian beams, such as could be caused by aberrations or by the overlap of the tweezers at small separations. The observed dipole–dipole interaction rate shown in Fig. 2 is faster by 17% than expected from the dipole moment of NaCs³⁸, which could be explained by a systematic error of 4% in this distance calibration.

Data availability

All data presented in this paper are available in the Harvard Dataverse⁷¹. Other supporting data are available from the corresponding author upon reasonable request.

Code availability

The code used for modelling in this study is available in the Harvard Dataverse⁷¹.

- Zhang, J. T. et al. Forming a single molecule by magnetoassociation in an optical tweezer. *Phys. Rev. Lett.* **124**, 253401 (2020).
- Picard, L. R. B. et al. High resolution photoassociation spectroscopy of the excited $c^3\Sigma_1^+$ potential of $^{23}\text{Na}^{133}\text{Cs}$. *Phys. Rev. Res.* **5**, 023149 (2023).
- Boradjiev, I. I. & Vitanov, N. V. Control of qubits by shaped pulses of finite duration. *Phys. Rev. A* **88**, 013402 (2013).
- Clopper, C. J. & Pearson, E. S. The use of confidence or fiducial limits illustrated in the case of the binomial. *Biometrika* **26**, 404–413 (1934).
- Sackett, C. A. et al. Experimental entanglement of four particles. *Nature* **404**, 256–259 (2000).
- Kramer, S., Plankensteiner, D., Ostermann, L. & Ritsch, H. QuantumOptics.jl: a Julia framework for simulating open quantum systems. *Comput. Phys. Commun.* **227**, 109–116 (2018).
- Singh, R. K., Senthilkumaran, P. & Singh, K. Tight focusing of vortex beams in presence of primary astigmatism. *J. Opt. Soc. Am. A* **26**, 576–588 (2009).
- Colbert, D. T. & Miller, W. H. A novel discrete variable representation for quantum mechanical reactive scattering via the S-matrix Kohn method. *J. Chem. Phys.* **96**, 1982–1991 (1992).
- Bezanson, J., Edelman, A., Karpinski, S. & Shah, V. B. Julia: a fresh approach to numerical computing. *SIAM Rev.* **59**, 65–98 (2017).
- Haegeman, J. Krylovkit (v0.8.1). *Zenodo* <https://doi.org/10.5281/zenodo.12122079> (2024).
- Efron, B. & Tibshirani, R. J. *An Introduction to the Bootstrap* (Chapman and Hall, 1994).
- Picard, L. R. et al. Experimental data and simulation code for Entanglement and iSWAP gate between molecular qubits. *Harvard Dataverse* <https://doi.org/10.7910/DVN/3UEBEV> (2024).
- Holland, C. M., Lu, Y., Li, S. J., Welsh, C. L. & Cheuk, L. W. Demonstration of erasure conversion in a molecular tweezer array. Preprint at <https://arxiv.org/abs/2406.02391> (2024).

Acknowledgements We thank J. Zhang for early experimental contributions; T. Rosenband, G. Pupillo, S. Jandura, M. Bergonzoni and B. Zhu for their discussions; and A. Carroll and A. Carter for careful reading of the paper. This work is supported by AFOSR (FA9550-23-1-0538), NSF (PHY-2110225 & PFC-PHY-2317149) and AFOSR-MURI (FA9550-20-1-0323 and FA9550-21-1-0069). Note that ref. 72 is a related molecule work leveraging hyperfine states as qubits.

Author contributions L.R.B.P. and A.J.P. collected and analysed the data. G.E.P. assisted with the data collection and developed molecular structure and aberration models. S.G. provided experimental support. D.W. performed the theoretical work and numerical modelling. A.M.R. supervised the theoretical work. K.-K.N. proposed and supervised the experiment. All authors contributed to the preparation of the paper.

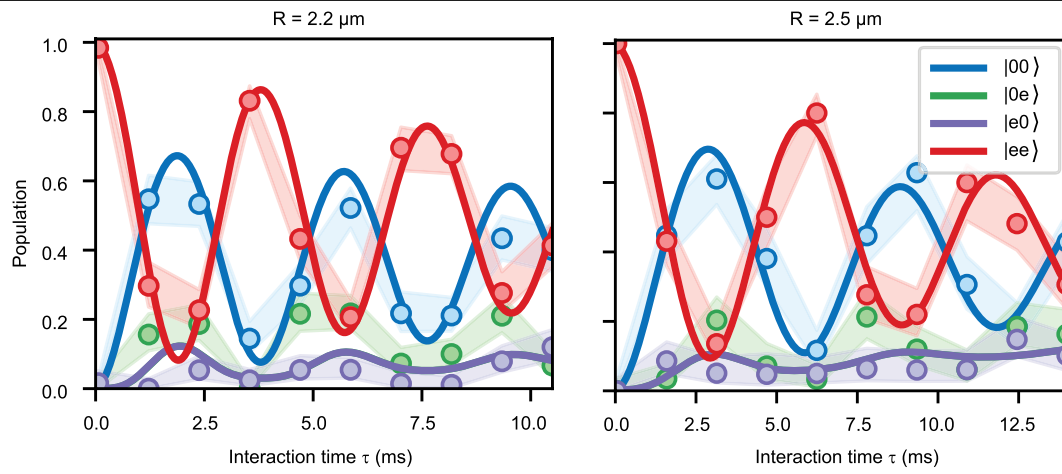
Competing interests The authors declare no competing interests.

Additional information

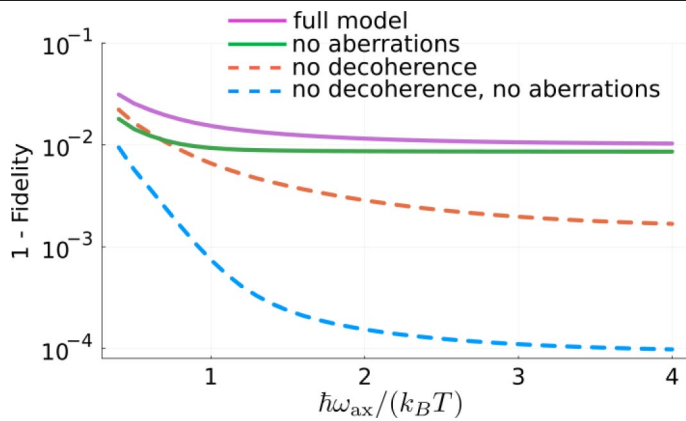
Correspondence and requests for materials should be addressed to Annie J. Park or Kang-Kuen Ni.

Peer review information *Nature* thanks the anonymous reviewers for their contribution to the peer review of this work.

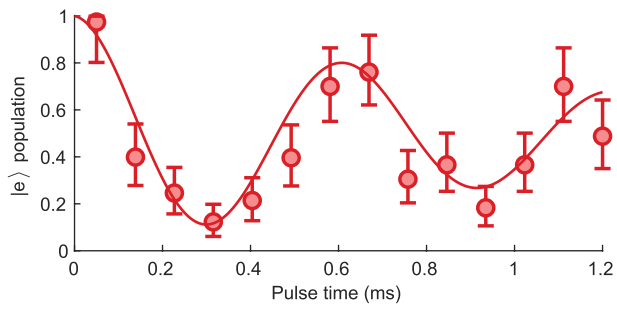
Reprints and permissions information is available at <http://www.nature.com/reprints>.



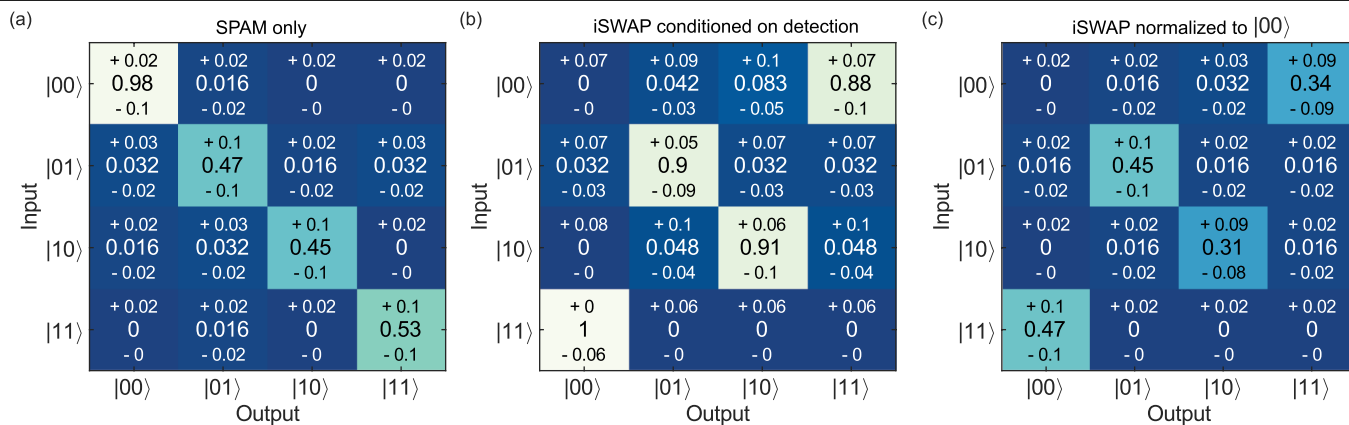
Extended Data Fig.1 | Dipole-dipole interactions using the same sequence as illustrated in Fig. 2 for intermolecular distances of 2.2 and 2.5 μm . Solid lines are fits to a master equation model of interaction with phenomenological dephasing parameters.



Extended Data Fig. 2 | Bell state infidelity at the optimal time predicted as a function of inverse temperature. The solid purple curve illustrates the prediction of the full model including astigmatism of 0.13λ . The green curve illustrates the corresponding result without any astigmatism. The two dashed curves show simulations without single-molecule decoherence $\gamma_{\text{deph}} = 0$, with (orange) and without (blue) astigmatism. Numbers quoted in the main text at 80% ground state fraction correspond to $\hbar\omega_{ax}/(k_B T) = 1.6$. Computed with motional level cutoffs $n = 25$ [$\hbar\omega_{ax}/(k_B T) = 0.4$]; $n = 20$ [$0.5 \leq \hbar\omega_{ax}/(k_B T) \leq 1.2$]; $n = 15$ [$1.3 \leq \hbar\omega_{ax}/(k_B T) \leq 2$]; $n = 10$ [$2 \leq \hbar\omega_{ax}/(k_B T)$].

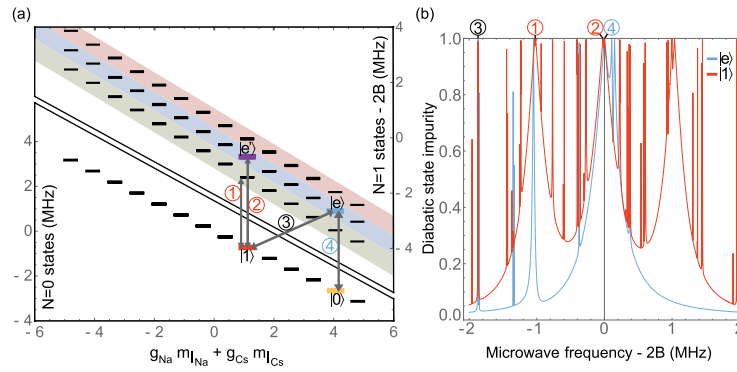


Extended Data Fig. 3 | Hyperfine-changing microwave pulse from $|e\rangle$ to $|1\rangle$. Fit is a \cos^2 function with symmetric exponential decay, giving a π -time of 0.307(9) ms and $1/e$ decay time of 1.2(4) ms.



Extended Data Fig. 4 | Full outcomes of truth table measurements for hyperfine gate. (a) Populations measured in each two-qubit state following state-preparation in that state, relative to population in $|00\rangle$, representing the relative SPAM fidelity of each state. (b) Populations measured in each two-qubit state as a fraction of the total detected molecule population in the

$(|0\rangle, |1\rangle)$ manifold for each of the input states to the iSWAP gate. This corrects for leakage to the $|e\rangle$ state during state-preparation and measurement, as well as during the hyperfine gate itself. (c) Populations measured in each two-qubit state following application of the iSWAP gate sequence, relative to the initial population in $|00\rangle$ in (a), illustrating the amount lost to leakage.



Extended Data Fig. 5 | Rotational-hyperfine structure and relevant coupling strengths of NaCs in the experimental regime. (a) Hyperfine sublevels of $N=0$ and $N=1$ rotational manifolds. Color-shaded regions denote states of the same rotational sub-level. The x-axis represents the combined nuclear-spin contribution to the Zeeman shift, and is chosen to make the rotational structure apparent. (b) Estimated impurity of the states $|1\rangle$ and $|e\rangle$

when dressed by the microwave field used for the $|1\rangle \leftrightarrow |e\rangle$ transition, which depicts all available transitions from these states. The hyperfine-changing transition, labeled by 3, is red-detuned from $|0\rangle \leftrightarrow |e\rangle$, labelled 4, by 1.9 MHz and comparably narrow. Off-resonant coupling is primarily due to the transitions 1, 2, and 4.

Extended Data Table 1 | Fit values and bootstrapped uncertainty estimates for master equation model of interactions, for the three distances shown in Fig. 2 and Extended Data Fig. 1

Separation (μm)	J/h (Hz)	δ/h (Hz)	γ_J (Hz)	γ_δ (Hz)	γ_Δ (Hz)
1.9	715(2)	17(17)	107(10)	25(3)	13(2)
2.2	477(3)	214(111)	125(29)	31(31)	16(16)
2.5	314(6)	159(159)	114(32)	53(53)	35(35)

The bootstrapped distributions of fit values for the master equation dephasing rates and detuning $|\delta|$ are in some cases consistent with zero to within 1σ , and are truncated below zero due to the restriction that values must be positive. In these cases we report the value as 1σ above zero, but note that the distribution deviates from Normal due to the truncation.